Supporting Information:

Advanced Average Power Factor and ZT Value in PbSe Thermoelectric with Dual Interstitials Doping

Liqing Xu,[a,b] Xiaoying Wang,[b] Yang Wang,[b] Zhibin Gao,[b] Xiangdong Ding,[b] and Yu Xiao[a,*]

[a]*School of Materials and Energy, University of Electronic Science and Technology of China, Chengdu 611731, China. E-mail: xiaoyu@uestc.edu.cn;*
[b]*State Key Laboratory for Mechanical Behavior of Materials, Xi'an Jiaotong University, Xi'an 710049, China.*

Experimental details

Synthesis: High purity raw materials, Pb bulk (99.999%), Se particles (99.999%), Te bulk (99.999%) and Cu wires (99.99%) with stoichiometric composition were weighted and flame-sealed in silica tubes at a residual pressure below ~ 10^{-4} Torr, slowly heated to 1323 K in 12 h and kept at this temperature for 6 h followed by furnace cooling to room temperature. The obtained ingots were ground into powders and densified by hot-pressing furnace (OTF-1700X-RHP4) at 773 K for 35 mins in a Φ 15 mm cylindrical die under an axial compressive stress of 50 MPa in vacuum, resulting in highly densified disk-shaped samples. Finally, the disk-shaped samples were annealed in vacuum at 773 K for 6 h.

Structural characterization: The phase identification was characterized through powder X-ray diffraction with Cu Kα ($\lambda = 1.5418$ Å) radiation in a reflection geometry operating at 40 kV and 40 mA. The lattice parameters were calculated and refined by using the software package which named "Materials Analysis using Diffraction (MAUD)". The scanning transmission electron microscopy (STEM) analysis was performed using a Cs-corrector JEM-ARM200F NEOARM with a cold FEG at 200 kV. The thin samples for transmission electron microscopy were prepared by the following methods, including cutting, grinding, polishing and Ar-ion milling on a liquid nitrogen cooling stage.

Density functional theory (DFT) calculations: The charge density and electron local density (ELF) are calculated by using the Vienna ab initio simulation package (VASP).[1, 2] The projector-augmented wave (PAW) potentials method[3] was utilized with Perdew-Burke-Ernzerhof (PBE) functional revised for solids to describe the exchange-correlation functional.[4] A cutoff energy of 400 eV was selected for the calculations. The unit cell was fully optimized until the force on each atom was less than 10^{-6} eV Å^{-1}. A k-point of $11 \times 11 \times 11$ was used and the total energy convergence criterion was set to 10^{-8} eV. To accurately simulate experimental local electron density, we constructed a preliminary $3 \times 3 \times 3$ supercell, which accommodated 216 atoms. This supercell was used to calculate the pure PbSe and PbSe with different types of defects, considering

Cu interstitial doping, Pb interstitial doping, and Se vacancy.

Thermoelectric transport properties measurements: The obtained highly-densified hot-pressing (HP) processed disk-shaped samples were cut into bars with dimensions around ~11.5 mm × 4 mm × 4 mm to measure electrical conductivity (σ) and Seebeck coefficient (S) in 300-773 K by using a CTA-3 (Cryoall, China) equipment under a low-pressure helium atmosphere. The HP disk-shaped samples were cut and polished into a square with sizes of ~8 mm × 8 mm and ~1.5 mm thickness for thermal diffusivity (D) measurements. The samples were coated with a thin graphite layer to minimize errors from the emissivity method in CLA-1000 (Cryoall, China) instrument. The sample density (ρ) was determined using the dimensions and mass of the samples. The specific heat capacity (C_p) was calculated by the Debye model. The thermal diffusivity data was analyzed using a Cowan model with pulse correction.

Lorenz number calculation. According to the Single Parabolic Band (SPB) model, the Lorenz number (L) is used to evaluate the electronic thermal conductivity (κ_{ele}) with a Wiedemann-Franz law of $\kappa_{ele} = L\sigma T$, where the σ is the electrical conductivity, T denotes working temperature. The L can be obtained by fitting the Seebeck coefficient (S) to the reduced chemical potential (η) with following equations:

$$L = \left(\frac{k_B}{e}\right)^2 \left(\frac{(r+7/2)F_{r+5/2}(\eta)}{(r+3/2)F_{r+1/2}(\eta)} - \left[\frac{(r+5/2)F_{r+3/2}(\eta)}{(r+3/2)F_{r+1/2}(\eta)}\right]^2 \right) \tag{S1}$$

$$S = \pm \frac{k_B}{e} \left(\frac{(r+5/2)F_{r+2/3}(\eta)}{(r+3/2)F_{r+1/2}(\eta)} - \eta \right) \tag{S2}$$

where the $F_n(\eta)$ is the n-th order Fermi integral:

$$F_n(\eta) = \int_0^\infty \frac{x^n}{1+e^{x-\eta}}dx \tag{S3}$$

$$\eta = \frac{E_F}{k_B T} \tag{S4}$$

where k_B, e and E_F denotes the Boltzmann constant, electron charge and Fermi level, r is the scattering factor, and the acoustic phonon scattering has been assumed as the main carrier scattering mechanism with $r = -1/2$.

Heat capacity calculation. The heat capacity in this work was theoretically evaluated by Debye model. The Debye model considers the individual contributions of phonons and effects of thermal expansion of lattice. The temperature-dependent total heat capacity ($C_{p, tot}$) can be obtained with following relationships:

$$C_{p, tot} = C_{p, ph}(T) + C_{p, D}(T) \tag{S5}$$

where $C_{p, ph}$ and $C_{p, D}$ denote heat capacity originated from phonon and lattice dilation, respectively. The phonon heat capacity $C_{p, ph}$ can be calculated by:

$$C_{p, ph}(T/\Theta_D) = 9R\left(\frac{T}{\Theta_D}\right)^3 \int_0^{\Theta_D/T} \frac{x^4 e^x}{\left(e^x - 1\right)^2} dx \tag{S6}$$

where Θ_D is Debye temperature, R is molar gas constant, $x = \hbar\omega/k_B T$, in which $\hbar$ and ω denotes reduced Planck constant and phonon vibration frequency, respectively.

The effects of lattice dilation on heat capacity $C_{p, D}$ can be obtained from:

$$C_{p, D}(T) = C_{ele, D}(T) + C_{ph, D}(T) = \frac{9BT\alpha^2}{10^6 \rho} \tag{S7}$$

where B is the isothermal bulk modulus, α is the linear coefficient of thermal expansion, and ρ is sample density. Notably, the electron heat capacity is not taken into account due to its negligible effects on lattice dilation compared with phonon.
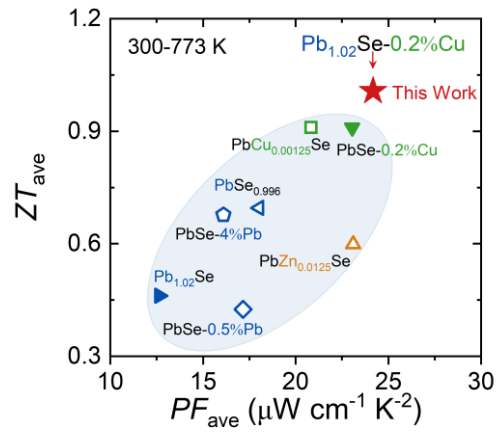
Figure S1. Comparison of ZT_{ave} and PF_{ave} values in *n*-type PbSe thermoelectric materials with interstitial doping at 300-773 K.
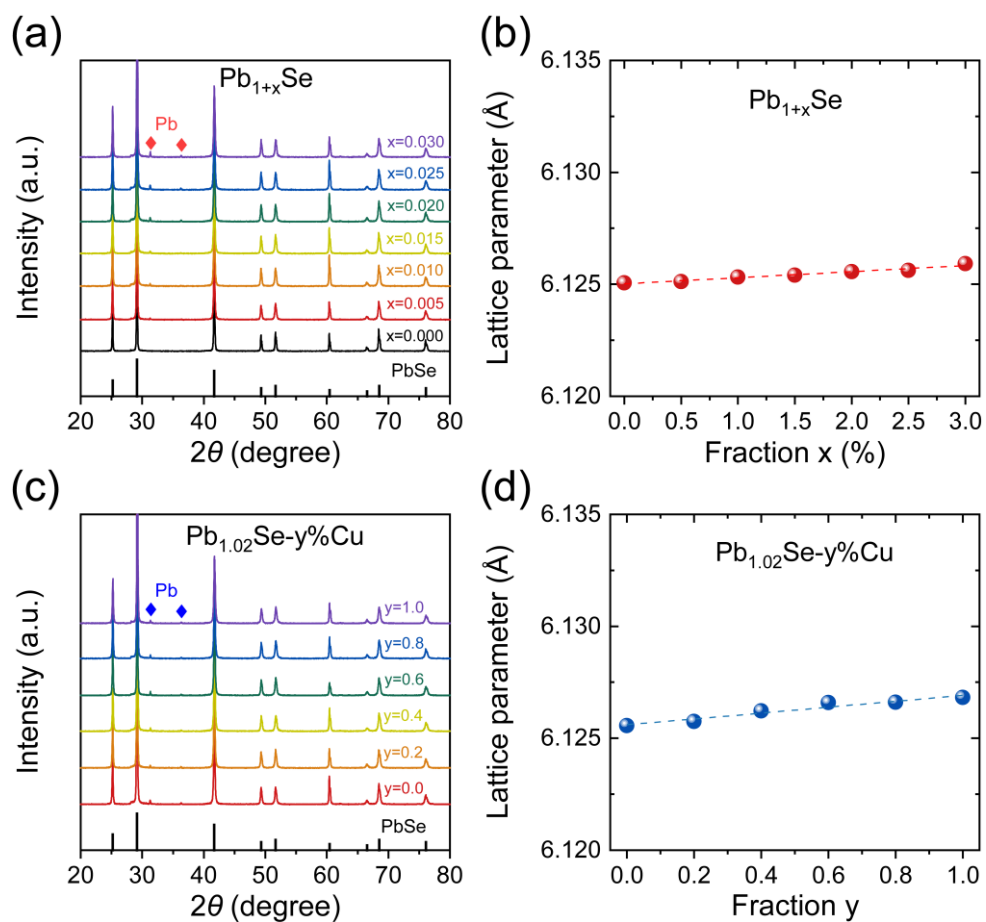
Figure S2. Phase identification of $Pb_{1+x}Se$ (x = 0.00-0.03) and $Pb_{1.02}Se$-y%Cu (y = 0.0-1.0): (a) PXRD patterns; (b) lattice parameter as a function of fraction x (%); (c) PXRD patterns; (d) lattice parameter as a function of fraction y.
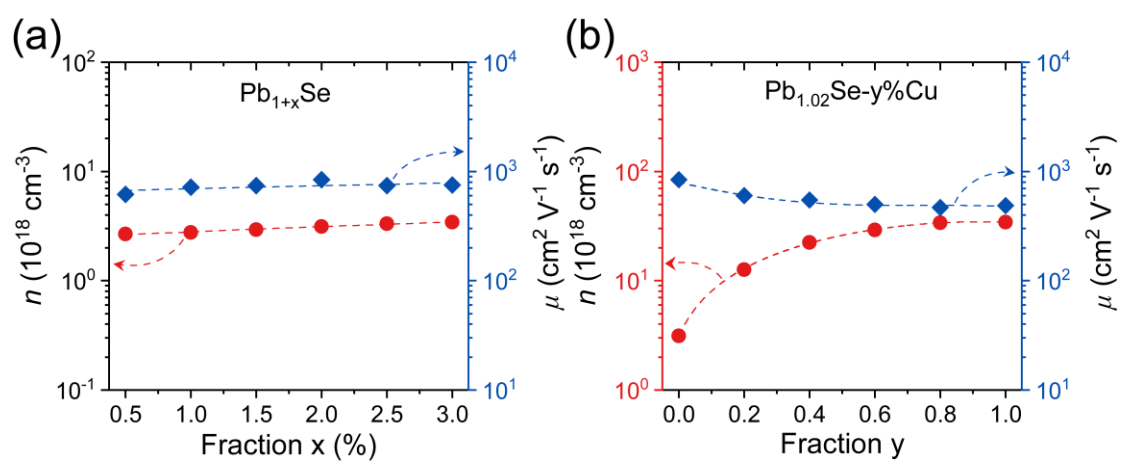
Figure S3. Electrical transport properties in $Pb_{1+x}Se$ (x = 0.005-0.030) and $Pb_{1.02}Se$-y%Cu (y = 0.0-1.0): (a) room-temperature carrier density and carrier mobility as a function of fraction x (%); (b) room-temperature carrier density and carrier mobility as a function of fraction y.
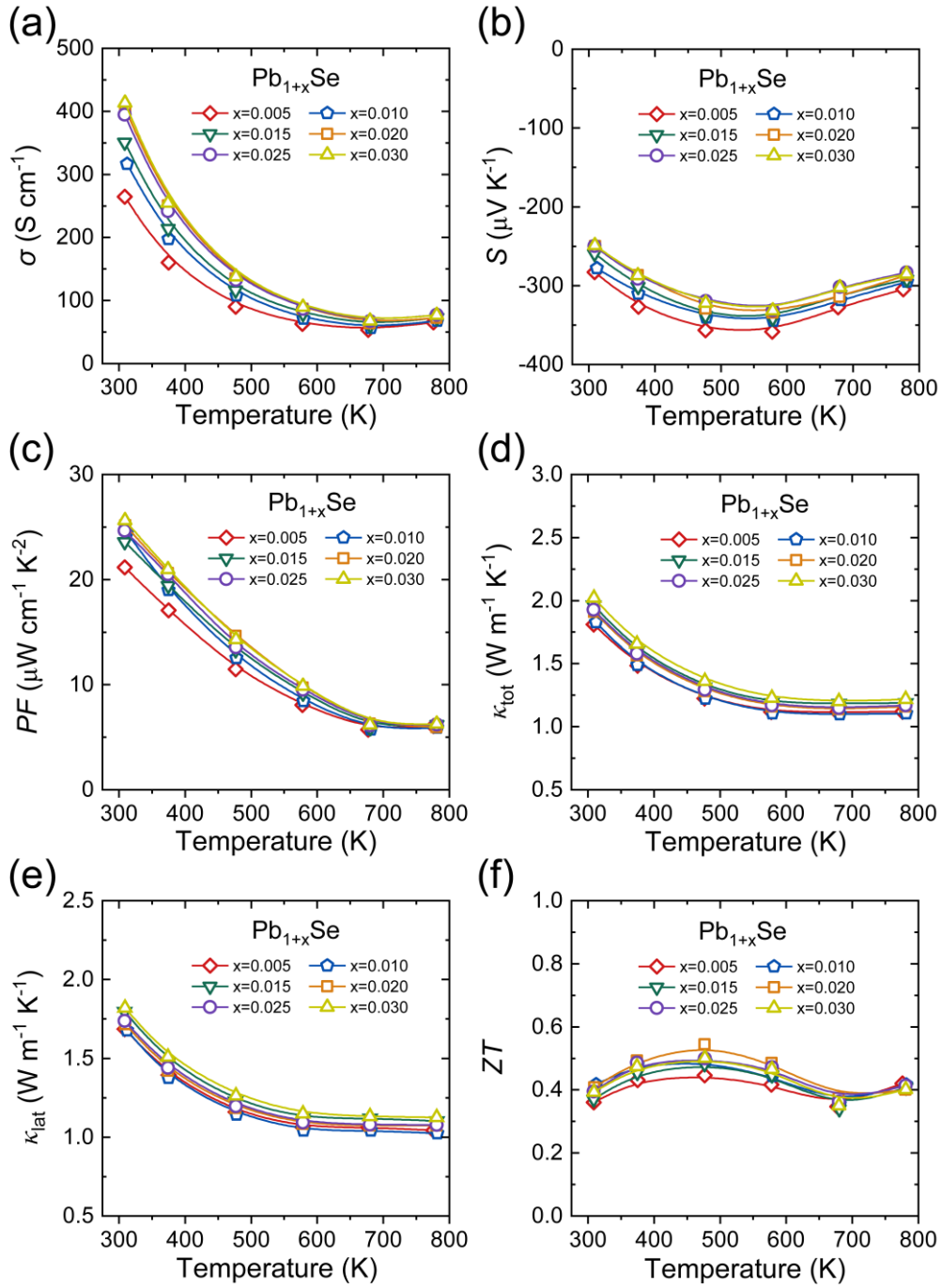
Figure S4. Thermoelectric transport properties in Pb$_{1+x}$Se (x = 0.005-0.030): (a) electrical conductivity; (b) Seebeck coefficient; (c) power factor; (d) total thermal conductivity; (e) lattice thermal conductivity; (f) *ZT* values.
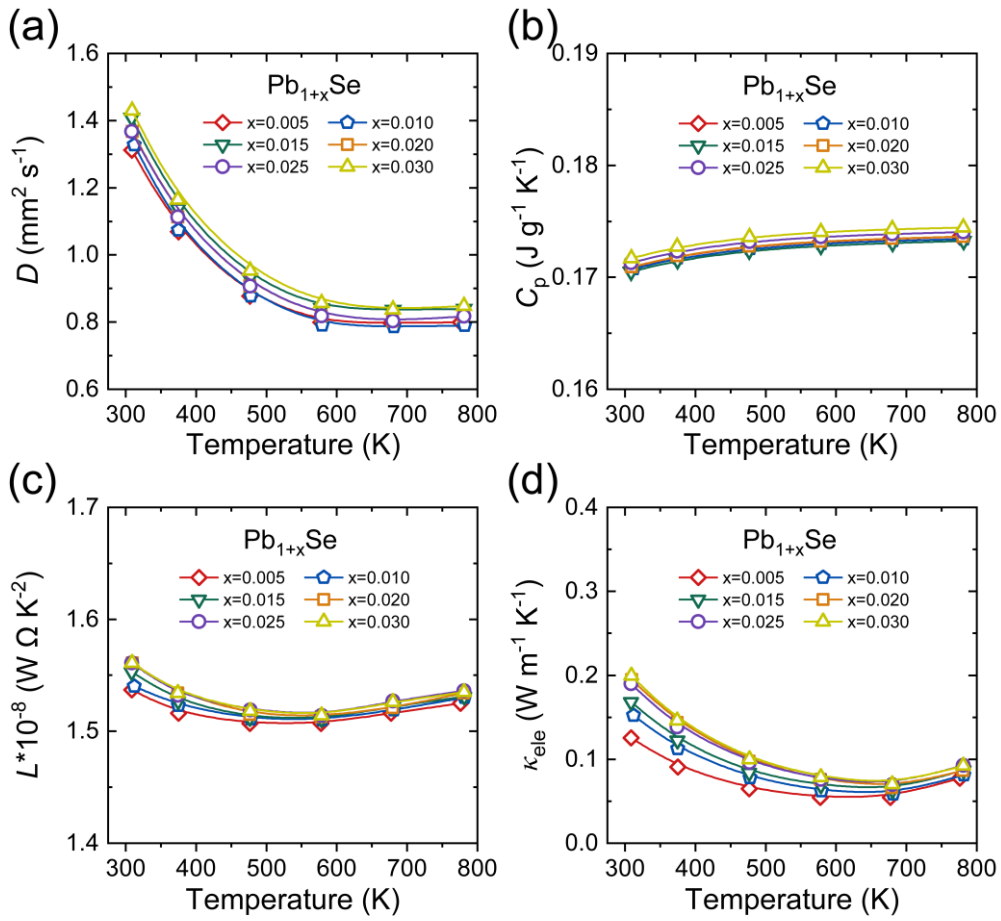
Figure S5. Thermoelectric properties in $Pb_{1+x}Se$ (x = 0.005-0.030): (a) thermal diffusivity; (b) heat capacity; (c) Lorenz number; (d) electronic thermal conductivity.
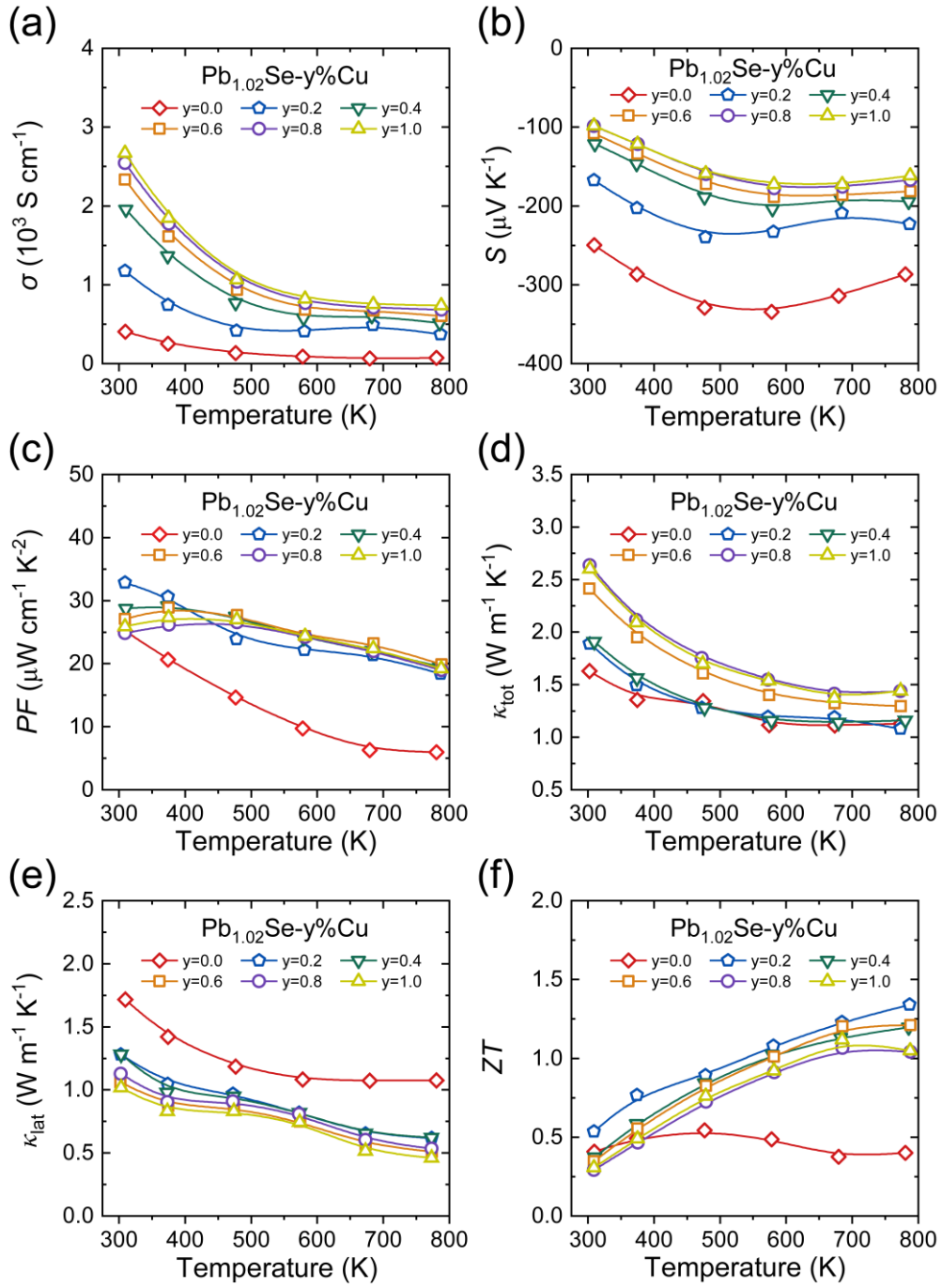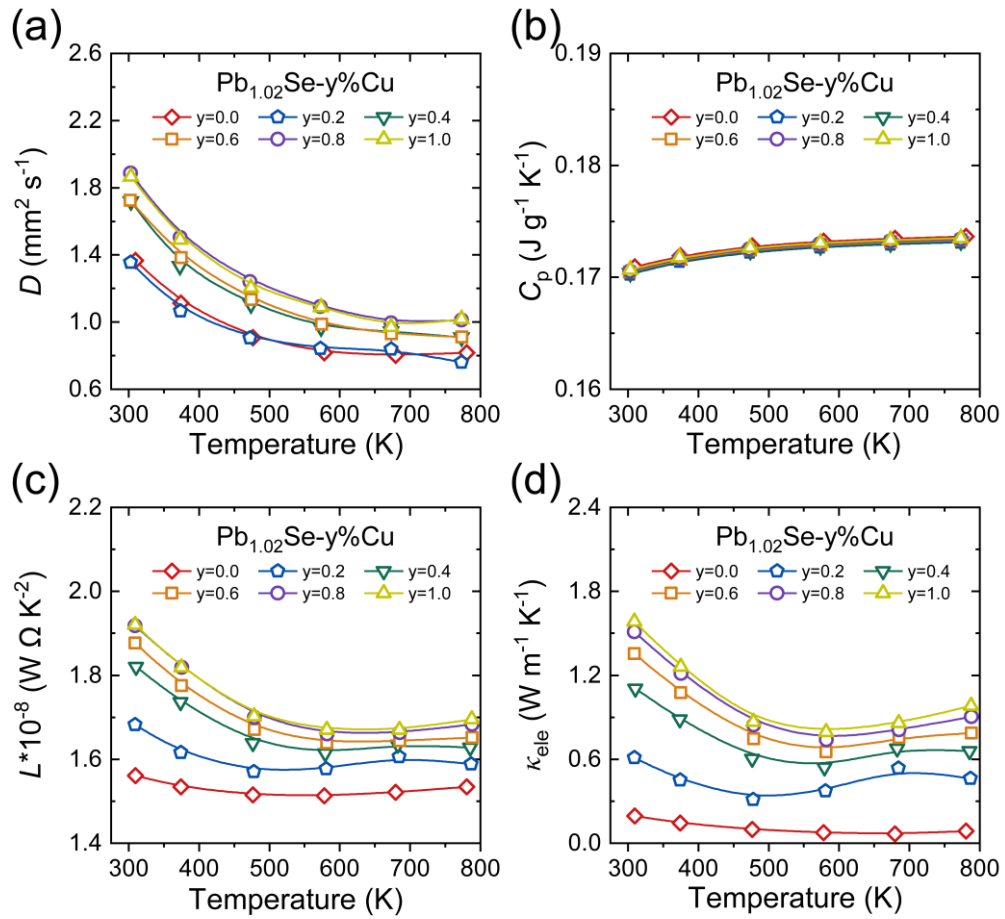
Figure S6. Thermoelectric transport properties in $Pb_{1.02}Se$-y%Cu (y = 0.0-1.0): (a) electrical conductivity; (b) Seebeck coefficient; (c) power factor; (d) total thermal conductivity; (e) lattice thermal conductivity; (f) *ZT* values.

Figure S7. Thermoelectric properties in Pb$_{1.02}$Se-y%Cu (y = 0.0-1.0): (a) thermal diffusivity; (b) heat capacity; (c) Lorenz number; (d) electronic thermal conductivity.
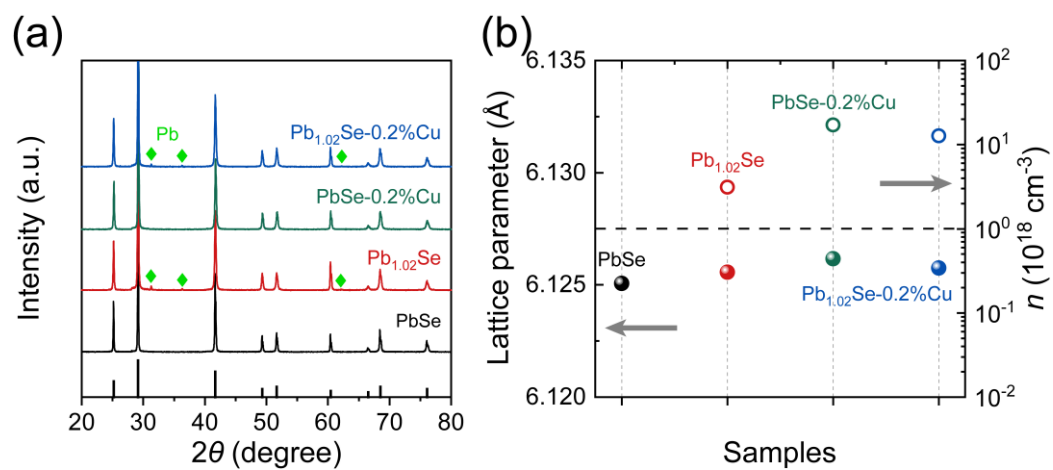
Figure S8. Phase identification and carrier density of PbSe, $Pb_{1.02}Se$, PbSe-0.2%Cu and $Pb_{1.02}Se$-0.2%Cu: (a) PXRD patterns; (b) lattice parameter and carrier density.
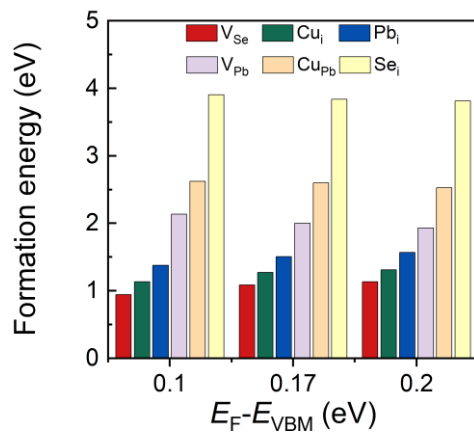
Figure S9. Defects formation energies for Pb-rich condition as a function of Fermi energy in PbSe. The conduction band minimum (CBM) is around ~0.17 eV.[5] The energy level is reference to the valence band maximum (VBM) of the host.[6]
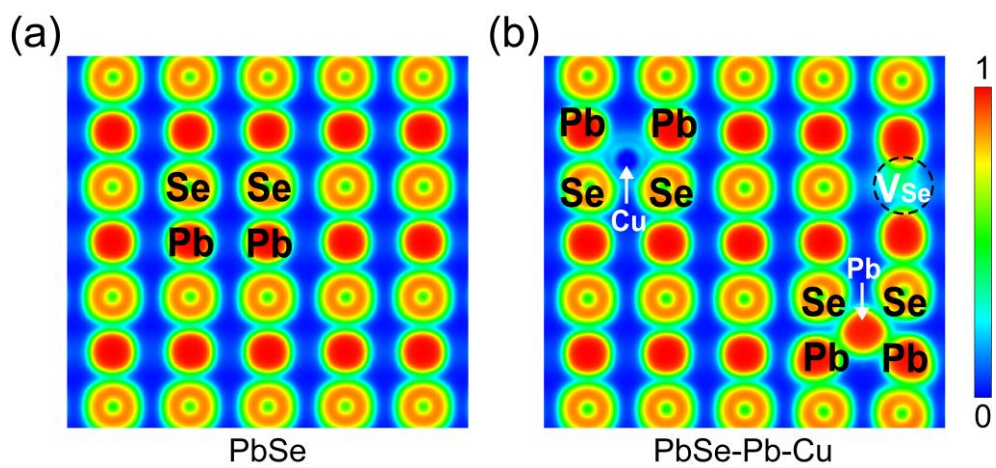
Figure S10. Electron localization functions (ELF) for (a) pristine PbSe and (b) PbSe with Pb interstitial, Cu interstitial and Se vacancy.
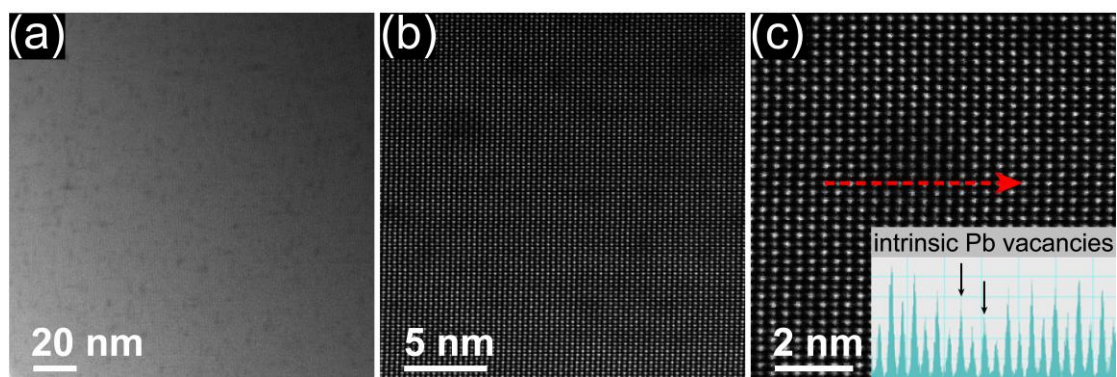
Figure S11. Microstructural characterization of the pristine PbSe: (a) the low magnification annular dark filed (ADF) image; (b) the enlarged STEM image; (c) the presence of a large number of intrinsic Pb vacancies.
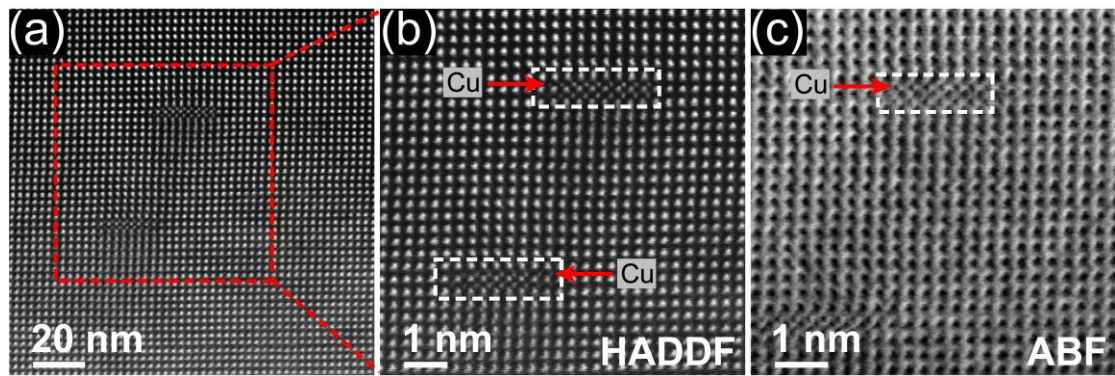
Figure S12. The Cu interstitial atoms observed from the [100] axis: (a) the low magnification annular dark filed (ADF) image; (b) the enlarged high angle annular dark field (HAADF) STEM image and (c) its corresponding annular bright field (ABF) STEM image.
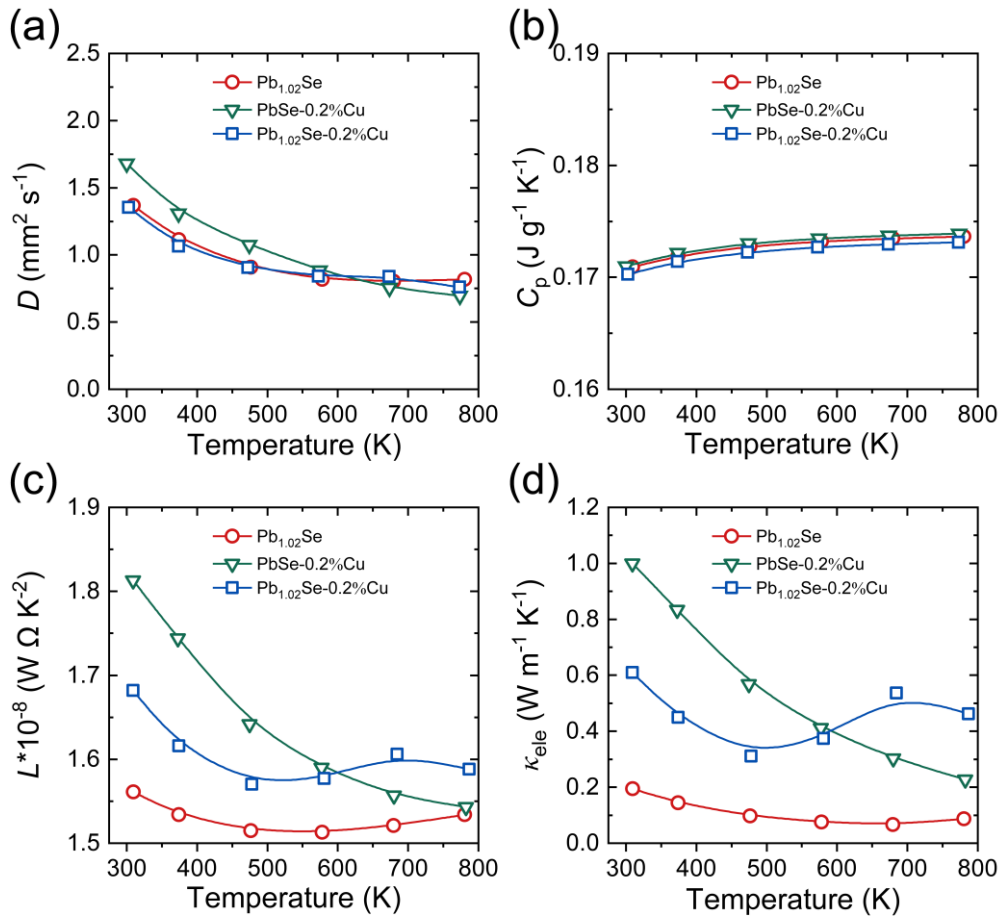
Figure S13. Thermoelectric transport properties in $Pb_{1.02}Se$, PbSe-0.2%Cu and $Pb_{1.02}Se$-0.2%Cu: (a) thermal diffusivity; (b) heat capacity; (c) Lorenz number; (d) electronic thermal conductivity.
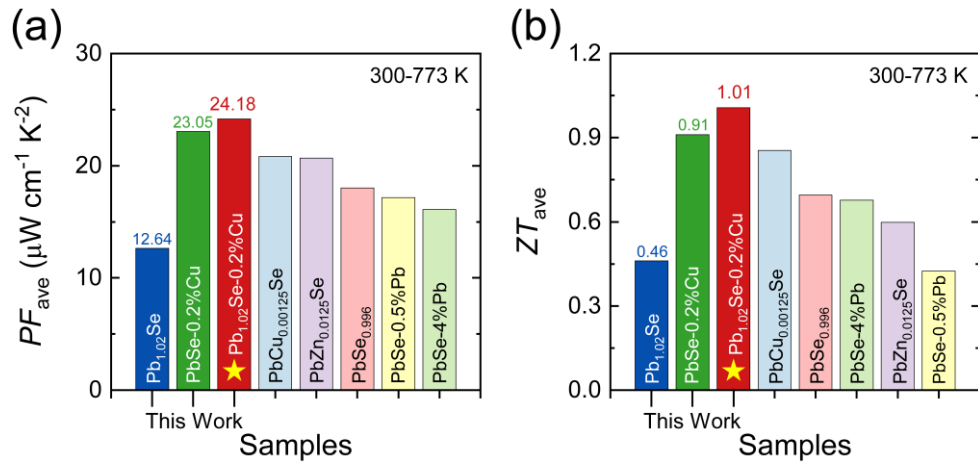
Figure S14. Comparison of thermoelectric transport performance in *n*-type PbSe-based thermoelectric materials with interstitial doping: (a) PF_{ave} values at 300-773 K; (b) ZT_{ave} values at 300-773 K.
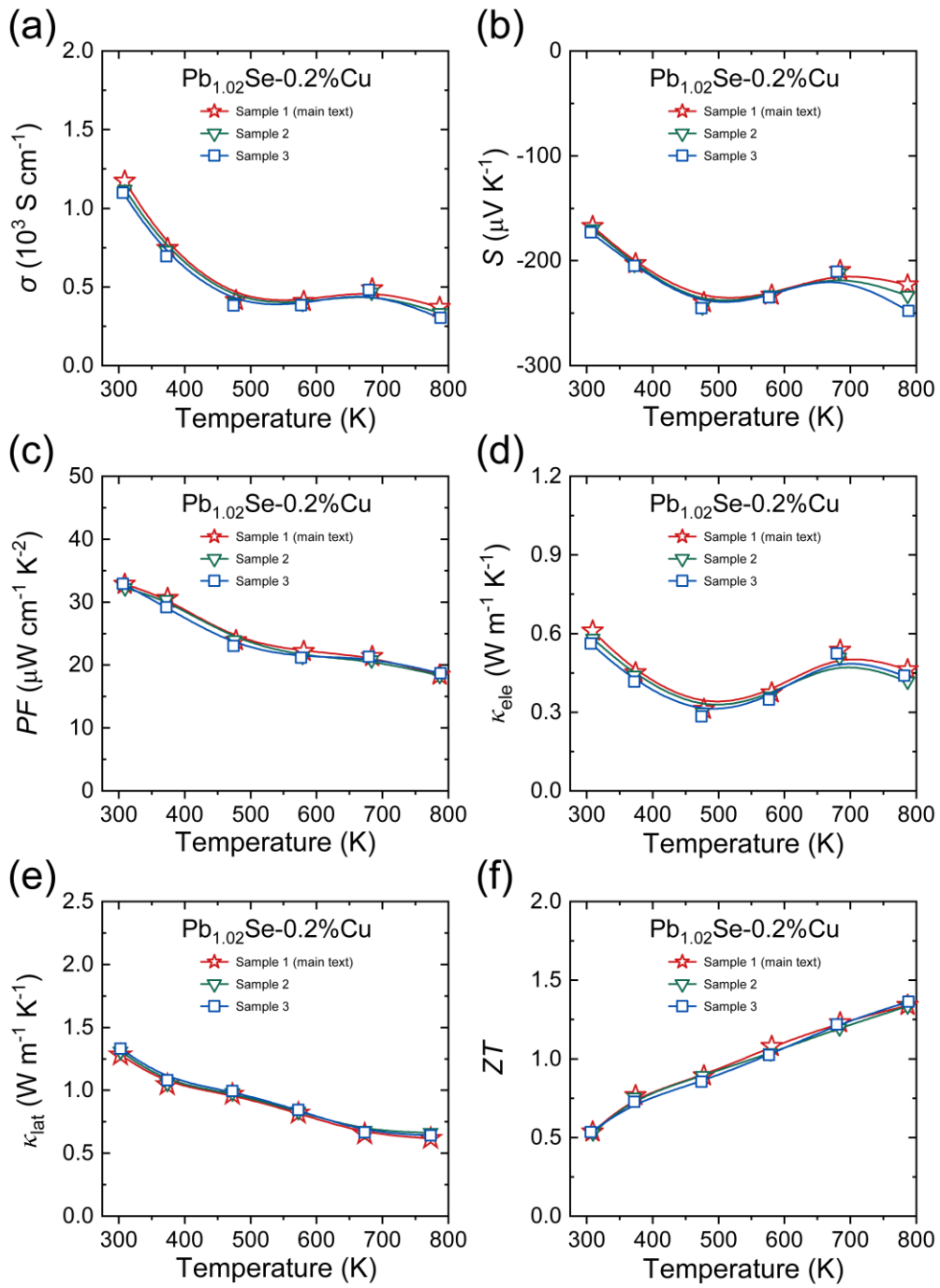
Figure S15. Reproducibility of the thermoelectric transport properties in $Pb_{1.02}Se$-0.2%Cu: (a) electrical conductivity; (b) Seebeck coefficient; (c) power factor; (d) electronic thermal conductivity; (e) lattice thermal conductivity; (f) *ZT* values.

Figure S16. Cycle tests of the thermoelectric transport properties in $Pb_{1.02}Se-0.2\%Cu$: (a) electrical conductivity; (b) Seebeck coefficient; (c) power factor; (d) electronic thermal conductivity; (e) lattice thermal conductivity; (f) *ZT* values.
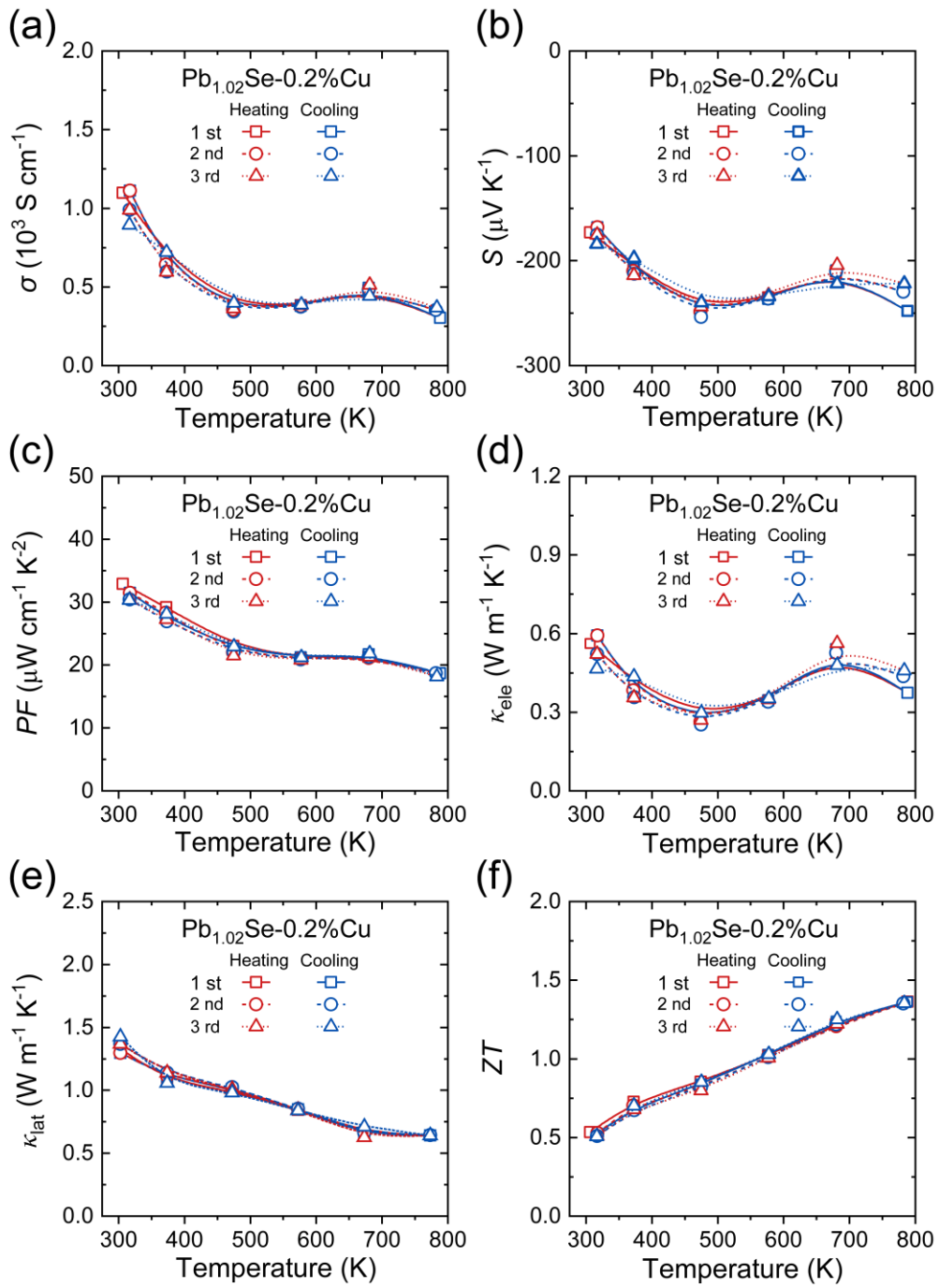
Table S1. Carrier density, effective mass, carrier mobility and density in $Pb_{1+x}Se$ (x = 0.005-0.030), PbSe-0.2%Cu and $Pb_{1.02}Se$-y%Cu (y = 0.2-1.0).

Samples		n (10^{18} cm^{-3})	m^* (m_e)	μ (cm^2 V^{-1} s^{-1})	ρ (g cm^{-3})
	x = 0.005	2.67	0.51	618.21	8.08
	x = 0.010	2.76	0.50	716.84	8.07
	x = 0.015	2.94	0.45	744.30	8.18
$Pb_{1+x}Se$	x = 0.020	3.13	0.44	843.40	8.18
	x = 0.025	3.32	0.45	741.84	8.23
	x = 0.030	3.43	0.46	751.32	8.23
PbSe-0.2%Cu		16.92	0.43	772.77	8.10
	y = 0.2	12.64	0.54	600.87	8.19
	y =0.4	22.36	0.51	546.60	8.15
$Pb_{1.02}Se$-y%Cu	y = 0.6	29.22	0.53	498.53	8.21
	y = 0.8	33.92	0.53	468.22	8.20
	y = 1.0	34.29	0.53	486.15	8.17

References

1. G. Kresse and J. Furthmüller, *Phys. Rev. B*, 1996, **54**, 11169.
2. G. Kresse and J. Furthmüller, *Comp. Mater. Sci.*, 1996, **6**, 15-50.
3. G. Kresse and D. Joubert, *Phys. Rev. B*, 1999, **59**, 1758.
4. J. P. Perdew, A. Ruzsinszky, G. Csonka, O. Vydrov, G. Scuseria, L. Constantin, X. Zhou and K. Burke, *Phys. Rev. Lett.*, 2008, **100**, 136406.
5. X. Qian, H. Wu, D. Wang, Y. Zhang, J. Wang, G. Wang, L. Zheng, S. Pennycook and L.-D. Zhao, *Energy Environ. Sci.*, 2019, **12**, 1969-1978.
6. X. Qian, D. Wang, Y. Zhang, H. Wu, S. Pennycook, L. Zheng, P. Poudeu and L.-D. Zhao, *J. Mater. Chem. A*, 2020, **8**, 5699-5708.